International Journal of Engineering and Technology sciences (IJETS) 2(6): 522-532, 2014
ISSN 2289-4152

Research Article

Comparison of iterative Fourier algorithms for wavefront reconstruction in adaptive optics systems

Abolhasan Mobashery[a], Morteza Hajimahmoodzadeh[a,b,*], Hamidreza Fallah[a,b]

[a] Department of physic, University of Isfahan, Isfahan, Iran
[b] [2]Quantum Optics Research Group, University of Isfahan, Isfahan, Iran
* Corresponding author. Tel.: +98-3137934824.; fax: +98-3137934800
E-mail address: morteza16@yahoo.com

A b s t r a c t

Keywords:

Adaptive optics, Wavefront reconstruction, Iterative Fourier reconstruction.

The accuracy of wavefront reconstruction from discrete slope measurements in adaptive optics (AO) systems depends on the sampling geometry, coherent length of the incoming wavefront, wavefront sensor specification and accuracy of the reconstruction algorithm. In this paper, simulation of Gaussian beam propagation in a turbulent atmosphere was carried out and the slope measured by Shack-Hartmann wavefront sensor (SHWS) was simulated. Wavefront reconstruction based on iterative discrete Fourier transforms was simulated, and then reconstructions with Fried and Hudgin inverse filter in spatial frequency domain were compared with Roddier iterative Fourier reconstruction. In these algorithms, no spatial boundary control is required. Our simulations showed that Hudgin algorithm results in a bigger Strehl ratio, so its reconstruction performance is more accurate than Fried and Roddier algorithms. In comparison to vector matrix multiplication reconstruction, this algorithm is faster and more accurate.

Accepted:27 December2014

1. Introduction

A beam of light propagating in a turbulent medium is aberrated because of local changes of index of refraction. Adaptive optics (AO) technology has been used to remove these dynamic aberrations of wavefront in real time. The basic idea of dynamic correction of wavefront was first proposed by Babcock in 1953 [1]. Although AO was initially developed for astronomical telescopes, it is now being used in several areas such as vision science, free space optical communications, optical microscopy , etc [2-4]. The three main components of an AO system are the wavefront sensor, which detects wavefront distortions; the correction component such as a deformable mirror (DM), which removes aberration of wavefront, and finally the control unit, which generates control signals of DM based on wavefront sensor measurements. A common wavefront sensor used in AO systems is the Shack-

Hartman wavefront sensor (SHWS) because of its simple optical structure and robustness. This sensor consists of an array of micro lenses placed in front of a detector array like a CCD. It can determine the local slope of input wavefront by measuring spots movements in the focal plane of each lenslet subaperture. The local slopes of wavefront are related to the wavefront phase by means of a set of linear equations, and the control unit generates proper signals for deformable mirror actuators by solving these equations. Vector matrix multiplication method (VMM) [5] and iterative Fourier transforms method (IFT) [6] are two methods used to solve these equations. The VMM method, in comparison to IFT, has many computation burdens, so it is not suitable for systems with a large number of mirror actuators and lenslets. If time interval between sensing and correction of wavefront is greater than the rate of turbulence's change, correction process adds more aberrations to the wavefront. The computation time of VMM is $O(n^2)$ while that of IFT is $O(n \ln n)$ in which n is the degree of freedom of system i.e. number of actuators [7]. Iterative algorithms are widely used in image processing and other aspects of science and technology because of its accuracy and speed [8]. Iterative algorithm is used in this article.

Using Fourier transforms to determine the wavefront phase from local slopes of wavefront was first proposed by Frischlad and Koliopoulus [6]. Since almost all telescopes have a circular aperture with central obscuration and Fourier transforms are defined on a rectangular grid point, using this method in a circular area generates a wavefront with many errors in aperture's boundary. Poyneer et al. used boundary and extension method to solve this problem in circular and annular apertures [9]. Before these methods, Roddier solved this problem based on Gerchberg–Saxton iteration method, which can be applied for each arbitrary aperture shape [10, 11].

In this paper, we study the wavefront reconstruction of an aberrated wavefront whose measurement is in a circular aperture based on IFT method. We have used two different sets of equations in IFT method and have compared the resulting wavefronts. One set is called Roddier – Gerchberg (RG), which is based on Roddier equation. The other set of equations is based on the sampling geometries of the aperture, i.e. Fried or Hudgin geometries; so, they are called Fried –Gerchberg (FG) and Hudgin – Gerchberg (HG) methods. IFT method and these equations will be explained in Section 2. In section 3 simulation of propagated wavefront in a turbulent atmosphere will be explained. SHWS and reconstruction process are also discussed in this section, and then the final results will be presented.

2. Wavefront reconstruction algorithm

In reconstruction algorithms, input function is the local slopes of wavefront measured by SHWS. In IFT algorithms, Fourier transforms of these slopes show their spectrum in the spatial frequency domain. Wavefront is then calculated in the frequency domain by using one of the equations which will be described later. By applying inverse Fourier transform, the wavefront will result in a spatial domain. The defined error function tells us whether the reconstructed wavefront is acceptable or not. Since the

available data are the slopes measured by SHWS in the actual AO system, the error function is defined based on the slopes:

$$\text{error} = \left[\frac{\sum_{i,j}\left(\left(\xi_{i,j}-\hat{\xi}_{i,j}\right)^2+\left(\eta_{i,j}-\hat{\eta}_{i,j}\right)^2\right)}{\sum_{i,j}\left(\left(\hat{\xi}_{i,j}\right)^2+\left(\hat{\eta}_{i,j}\right)^2\right)}\right]^{1/2} \quad (1)$$

Where $\xi_{i,j} = \frac{\partial S}{\partial x}\Big|_{x_i,y_j}$ and $\eta_{i,j} = \frac{\partial S}{\partial y}\Big|_{x_i,y_j}$ are slopes of wavefront obtained from reconstructed wavefronts and $\hat{\xi}_{i,j}$ and $\hat{\eta}_{i,j}$ are slopes measured by SHWS in each (x_j, y_j) point. If the reconstructed wavefront with a criterion selected based on the problem conditions is not acceptable, an iterative manner is used and the calculated slopes from reconstructed wavefront are replaced by the measured ones, and the algorithm is repeated. Since the output of SHWS is usually in a circular or annular area and Fourier Transforms are defined on a rectangular area, the replacement process solely involves the slopes in a circular area, and the slope outside this area will be unchanged. Figure 1 shows these two areas. The method of calculating local slopes of wavefront depends on the geometry of reconstruction, which will be explained in section 2.2. Figure 2 shows flow chart of this algorithm.

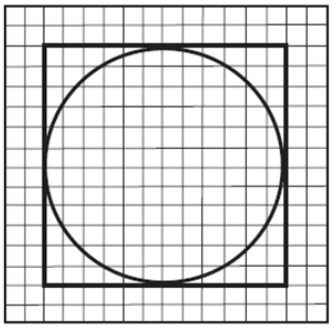

Fig. 1: The circular area shows measured slopes by SHWS and the rectangular area is an area defined for FFT

Another metric performance is defined to evaluate the ability of a wavefront reconstruction process. It is Strehl ratio for the two wavefronts of interest; U_1 and U_2, where U_1 is the wavefront to be measured, and U_2 is a reconstructed wavefront. The Strehl ratio is formed on a set of points:

$$SR = \frac{\left|\sum_{i,j} U_{1;i,j} U^*_{2;i,j}\right|^2}{\left[\sum_{i,j} U_{1;i,j} U^*_{1;i,j}\right]\left[\sum_{i,j} U_{2;i,j} U^*_{2;i,j}\right]} \quad (2)$$

Replacement of slopes is in a circular area enclosed by a rectangle since slopes measurements are in a circular aperture, and calculations take place on a rectangular array too.

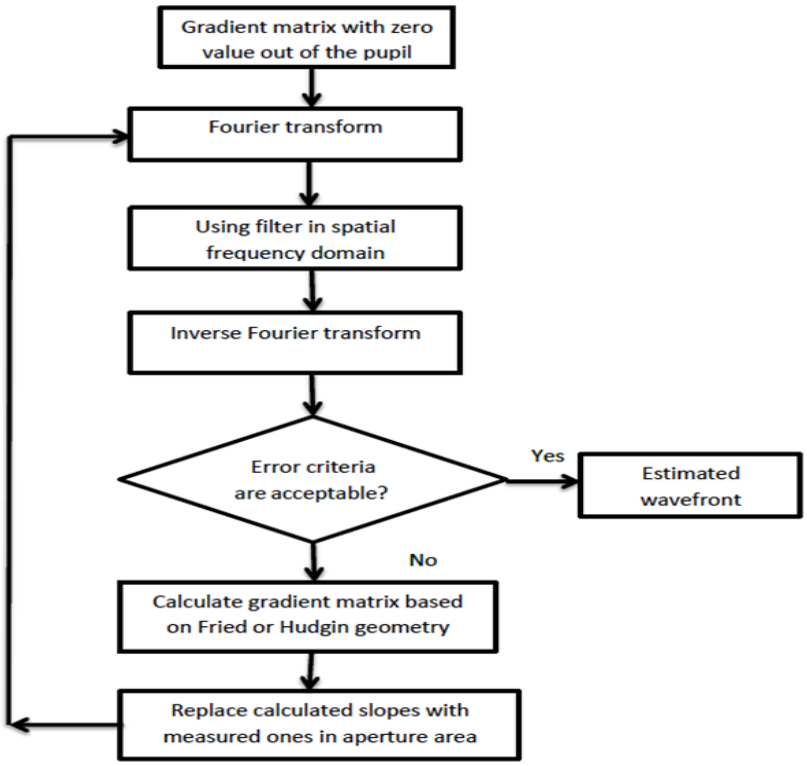

Fig. 2: Flow chart of iterative algorithm

2.1. RG algorithm

Consider wavefront $S(x, y)$ in Cartesian coordinate. It can be expanded as:

$$S(x,y) = \iint a(u,v)\exp[j2\pi(ux+vy)]dudv \quad (3)$$

Where (u, v) are spatial frequencies and $a(u, v)$ is the expansion coefficient of $S(x, y)$ in the spatial frequency domain. Derivation of equation (2) with respect to x and y gives:

$$\xi(x,y) = j2\pi \iint ua(u,v)\exp[j2\pi(ux+vy)]\, dudv \quad (4)$$

$$\eta(x,y) = j2\pi \iint va(u,v)\exp[j2\pi(ux+vy)]\, dudv \quad (5)$$

Since the derivative of a Fourier series is a Fourier series, we have:

$$\xi(x,y) = \iint b_u(u,v)\exp[j2\pi(ux+vy)]\, dudv \quad (6)$$

$$\eta(x,y) = \iint b_v(u,v)\exp[j2\pi(ux+vy)]\, dudv \quad (7)$$

Where $b_u(u, v)$ and $b_v(u, v)$ are coefficients of Fourier transform of $S(x, y)$ slopes. Comparing equation (4) with (6) and equation (5) with (7) results in:

$$a(u,v) = -j\frac{ub_u(u,v)+vb_v(u,v)}{2\pi(u^2+v^2)} \quad (8)$$

According to equation (8), starting from wavefront slopes i.e. $\xi(x,y)$ and $\eta(x,y)$, expansion coefficients of $S(x,y)$ can be calculated and then the $S(x,y)$ in the space domain can be achieved. Equation (8) is valid for an unbounded function; so, for error reduction at boundaries, an iterative method should be used to have a continuous slope on both sides of boundaries.

2.2. Phase and slop relation based on sampling geometry (FG and HG algorithms)

The local slopes of wavefront are measured in discrete positions by SHWS, and the control unit sends command signals to the mirror actuators based on these slopes. Fried and Hudgin geometries are two common geometries that relate the measured wavefront slopes to phase positions [12]. In Fried geometry, a set of points corresponding to the corners of the SH subaperture shows phase positions or mirror actuators. In Hudgin geometry, the set points for wavefront estimation are placed in the middle point of subaperture lines.

In Fried geometry, the average of two adjacent phase points is taken as a slope:

$$\xi_{i,j}^{(F)} = \left[\left(S_{i+1,j} + S_{i+1,j+1}\right) - \left(S_{i,j} + S_{i,j+1}\right)\right]/2h \tag{9}$$

$$\eta_{i,j}^{(F)} = \left[\left(S_{i,j+1} + S_{i+1,j+1}\right) - \left(S_{i,j} + S_{i+1,j}\right)\right]/2h \tag{10}$$

In Hudgin geometry, the difference between the adjacent phase points is taken as a slope:

$$\xi_{i,j}^{(H)} = \left[S_{i+1,j} - S_{i,j}\right]/h \tag{11}$$

$$\eta_{i,j}^{(H)} = \left[S_{i,j+1} - S_{i,j}\right]/h \tag{12}$$

Where $\xi_{i,j}$ and $\eta_{i,j}$ are slopes in (i,j) points, $S_{i,j}$ is phase in this point and h is the separation between adjacent points. Now, according to the geometry of reconstruction and by using these equations, wavefront slope can be calculated in the iterative algorithm.

Using discrete Fourier transform of phase-slope relations and the shift property of Fourier transform results in different equations that can be used in IFT. In Fried geometry, we have [9]:

$$\tilde{S}_{k,l} = \begin{cases} 0 & k,l = 0\ ,k,l = N/2 \\ \left\{\begin{matrix}\left[\exp\left(\frac{-j2\pi k}{N}\right) - 1\right]\left[\exp\left(\frac{j2\pi l}{N}\right) + 1\right]\tilde{\xi}_{k,l}^{(F)} + \\ \left[\exp\left(\frac{-j2\pi l}{N}\right) - 1\right]\left[\exp\left(\frac{j2\pi k}{N}\right) + 1\right]\tilde{\eta}_{k,l}^{(F)}\end{matrix}\right\} & \\ \times\left[8\left(\sin^2\left(\frac{\pi k}{N}\right)\cos^2\left(\frac{\pi l}{N}\right) + \sin^2\left(\frac{\pi l}{N}\right)\cos^2\left(\frac{\pi k}{N}\right)\right)\right]^{-1} & \end{cases} \tag{13}$$

Where $\tilde{\xi}_{k,l}^{(F)}$ and $\tilde{\eta}_{k,l}^{(F)}$ are Fourier transforms of $\xi_{i,j}^{(F)}$ and $\eta_{i,j}^{(F)}$ in (k,l) points, respectively, $\tilde{S}_{k,l}$ is Fourier transform of phase and N is the number of sampling points or number of subapertures.

A similar approach for Hudgin geometry results in [9]:

$$\tilde{S}_{k,l} = \begin{cases} 0 & k,l = 0 \\ \left\{\left[\exp\left(\frac{-j2\pi k}{N}\right) - 1\right]\tilde{\xi}_{k,l}^{(H)} + \left[\exp\left(\frac{-j2\pi l}{N}\right) - 1\right]\tilde{\eta}_{k,l}^{(H)}\right\} & \\ \quad \times \left[4\left(\sin^2\left(\frac{\pi k}{N}\right) + \sin^2\left(\frac{\pi l}{N}\right)\right)\right]^{-1} & \text{else where} \end{cases} \quad (14)$$

Where $\tilde{\xi}_{k,l}^{(H)}$ and $\tilde{\eta}_{k,l}^{(H)}$ are Fourier transforms of $\xi_{k,l}^{(H)}$ and $\eta_{k,l}^{(H)}$ in (k,l) points, respectively. Inverse Fourier transform of equations (13) and (14) result in the estimated wavefront.

Now, we have two sets of equations that we can use in IFT to reconstruct the wavefront. The first one, equation (8), is the result of wavefront expansion based on sinusoidal functions known as Roddier-Gerchberg (RG). The second set, equations (13) and (14), is the result of iterative Fourier transforms of slope-phase relations. Equation (13) is named Fried-Gerchberg (FG) and equation (14) refers to Hudgin-Gerchberg (HG) algorithms.

3. Simulation results and discussion

Numerical simulations are used to evaluate the performance of each set of equations in IFT algorithm. In these simulations, propagation, detection and reconstruction of Gaussian beam are considered. An optical beam with wavelength $\lambda = 0.5$ μm is propagated over a distance of 10 Km through a turbulent atmosphere. Turbulent atmosphere is simulated with 20 equally spaced random phase screens along the propagation path. Each screen represents a 0.5 Km thick turbulent atmosphere. All the phase screens consist of an N×N array. To avoid the aliasing problem caused by using a Fast Fourier Transform (FFT), simulation's parameters are chosen so that the relation $N \geq 2\lambda z/\Delta^2$ is satisfied; where N is the number of sampling points along one direction of screen, z is the propagation distance and Δ is the sampling step [13]. In our simulation, N is equal to 1024 and Δ is set to 1 mm.

Random phase screens are generated by a sub-harmonic method [14] based on Von-Karman statistics, whose outer scale is equal to 100m. Strength of the turbulence is controlled by the structure constant of index of refraction, C_n^2. Turbulent atmosphere simulated with 10 different C_n^2 ranges from 1.2×10^{-17} $m^{-2/3}$ to 1×10^{-16} $m^{-2/3}$. For each simulation, C_n^2 is set to a constant value along the entire propagation path. The Rytove variance $\sigma_{\chi R}^2$ and Fried parameter, r_0, for a plane wave propagated along such path are calculated by means of the following equations [15]:

$$\sigma_{\chi R}^2 = 0.307 \left(\frac{2\pi}{\lambda}\right)^{7/6} L^{11/6} C_n^2 \quad (15)$$

$$r_0 = 0.331 \left(\frac{\lambda^2}{C_n^2 L}\right)^{3/5} \quad (16)$$

Table 1 shows C_n^2, r_0 and $\sigma_{\chi R}^2$ values for our simulations. Based on this table, the simulated atmosphere is in a weak turbulence regime.

Table. 1: Parameters used for simulating atmosphere with different turbulence strength. The last column shows SHWS subaperture diameter to r_0 ratios

Cn^2 (× **10^{-16}** $m^{-2/3}$)	r_0	$\sigma_{\chi R}^2$	d/r_0		
			Lenslet number = 16	Lenslet number = 32	Lenslet number = 64
1	0.145	0.05	0.43	0.22	0.11
2.22	0.089	0.11	0.70	0.35	0.17
3.44	0.069	0.18	0.91	0.45	0.23
4.67	0.057	0.24	1.09	0.54	0.27
5.8	0.050	0.30	1.25	0.63	0.31
7.11	0.044	.036	1.40	0.70	0.35
8.33	0.041	0.43	1.54	0.77	0.39
9.56	0.037	0.49	1.67	0.84	0.42
10.78	0.035	0.55	1.80	0.90	0.45
12.00	0.033	0.62	1.92	0.96	0.48

Simulation of wavefront sensing is performed with three different SHWS with 16, 32 and 64 lenslets along the direction of telescope diameter. Array size of each subaperture for these SHWS is equal to 64×64, 32×32 and 16×16, respectively; and their f-number is equal to 24. Lenslet diameter ratio to Fried parameter for each SHWS is shown in Table 1. As can be seen, for C_n^2 greater than 3.44×10^{-16} $m^{-2/3}$, d/r_0 ratio for 16 sub apertures SHWS is greater than 1, then wavefront sensing with this SHWS in these turbulence strengths results in wrong wavefront sensing.

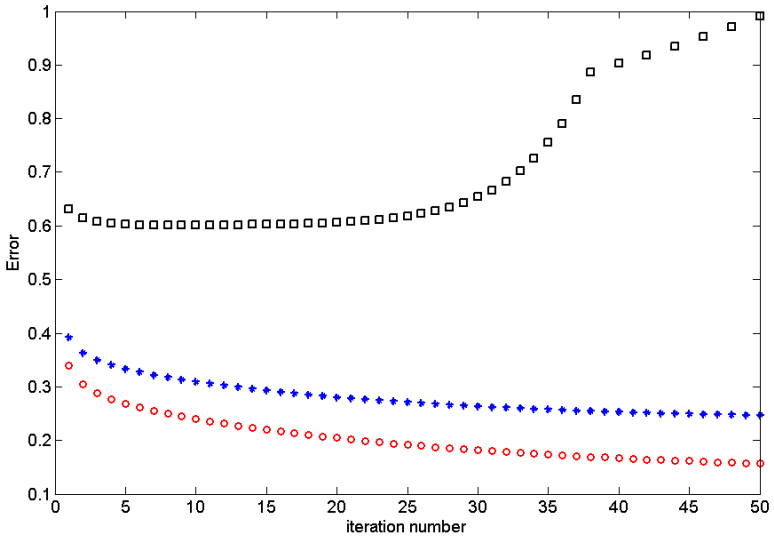

Fig. 3: Error of FG (circle), HG (stars) and RG (square) algorithms for the reconstruction of aberrated wavefront when it propagates in an atmosphere whose C_n^2 is equal to 1×10^{-16} $cm^{-2/3}$

The first part of our simulation includes a comparison of performance of equations (8), (13) and (14) for wavefront reconstruction on IFT algorithm. Error criteria of FG, HG and RG algorithms for propagated beam in atmosphere with turbulence strengths, Cn^2 , equals 1×10^{-16} $cm^{-2/3}$, as shown in Figure 3. In this figure, the horizontal axis shows iteration number and the vertical axis shows root mean square of slops difference relative to the square of reconstructed wavefront slopes. Error criteria for other Cn^2 values show a similar behaviour. As can be seen, FG algorithm has minimum errors, and errors of RG algorithm in a few initial iterations are reduced but they ultimately increase with an increase in the number of iterations. This figure shows FG and HG algorithms reconstruct the wavefront better than RG. An error criterion used to select the best iteration as a reconstructed wavefront is based on the slope difference between the desired and reconstructed wavefront. But the best metric for comparing these algorithms is Strehl Ratio (SR) that is shown in Figure 4. Strehl Ratio changes with increasing Fried parameter for different SHWS, which are characterized with their lenslet numbers, as shown in these figures. As expected, wavefronts reconstructed with RG algorithm show minimum SR and reconstructed wavefronts with HG show the best performance (bigger SR). This result is contrary to that of Figure 3 where FG algorithm has a better performance. It must be noticed that the error criterion in IFT algorithm based on the slope difference is used to stop the iteration process of reconstruction, but an AO system performance is evaluated based on SR. So, we can conclude that the HG algorithm has a better performance for wavefront reconstruction in a weak turbulence atmosphere.

As mentioned earlier, for SHWS with 16 lenslets along aperture diameter, d/r_0 ratio is smaller than 1, then wavefront sampling with this SHWS results in a wrong answer. Because of that, SR values of reconstructed wavefronts that sampled with this SHWS are smaller than others.

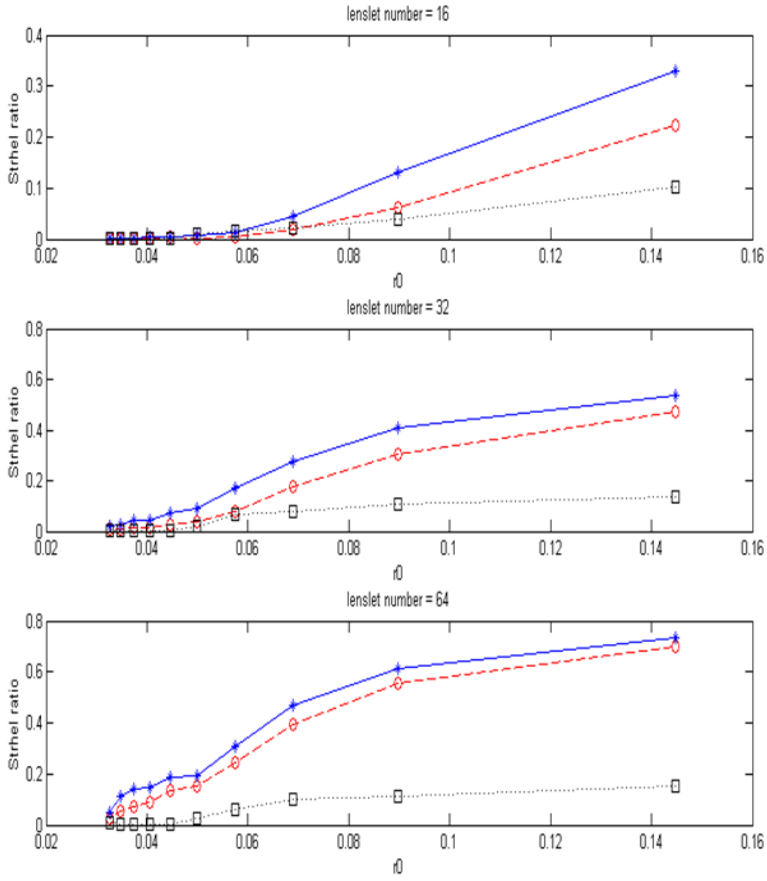

Fig. 4: Strehl ratio variation with r_0 for IFT reconstruction. In these figures (blue ○) shows Fried algorithm, (red *) shows Hudgin algorithm and (black □) shows Roddier algorithm. SHWS are characterized with their lenslet numbers in the direction of aperture diameter.

Comparison between VMM and IFT is the second part of our simulations. In VMM reconstruction, Fried and Hudgin geometries are used. Calculation of least square reconstruction was made practical by using the sparse matrix technique and Cholesky factorization. Performance metric for this comparison is SR, and Figure 5 shows SR variation with Fried parameter for all SHWS that are characterized with their lenslet numbers. Comparison between SR values in Figure 4 and Figure 5 shows that the IFT performance for wavefront reconstruction is better than VMM reconstruction in almost all turbulence strengths for weak turbulences.

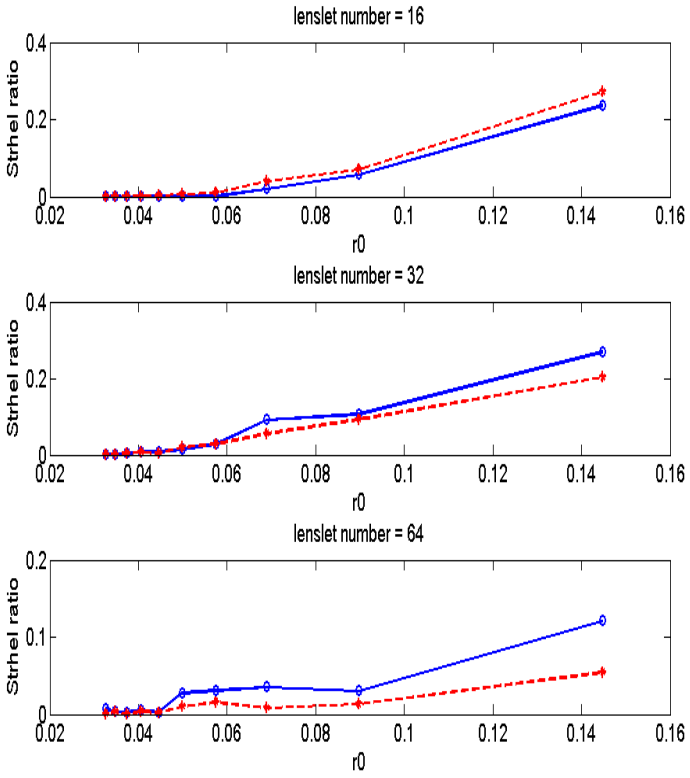

Fig. 5: Strehl ratio variation with r_0 for VMM reconstruction. In these figures (blue ○) shows Fried algorithm, (red *) shows Hudgin algorithm and (black □) shows Roddier algorithm. SHWS are characterized with their lenslet numbers in the direction of aperture diameter.

4. Conclusion

In this article, different IFT algorithms were used to reconstruct an aberrated wavefront in an AO system. In these algorithms, we used local slopes of wavefront that were measured by a SHWS as an input, and root square difference between measured slopes as an error criterion to terminate the iteration process. Another error criterion used was Strehl ratio. Hudgin and Fried geometry was used to calculate wavefront slopes in each iteration of algorithm, and three equations that relate wavefront phase in spatial space to frequency space were investigated. The first equation was Roddier and the other two were based on Fried and Hudgin geometry. Our simulations showed that the Hudgin algorithm reconstructs wavefront more accurately than algorithms based on Fried geometry and Roddier algorithm. Comparison between IFT and VMM algorithms show that the reconstruction wavefront with Hudgin geometry in IFT process has a better Strehl ratio.

Reference

[1] Babcock HW. The possibility of compensating astronomical; seeing. Publications of the Astronomical Society of the Pacific, 1953; 65(386): 229-236.

[2] Porter J, Queener H, Lin J, Thorn KE, and Awal A. Adaptive optics for vision Science: Principle, Practices, Design and Applications, Wiely 2006.

[3] Tyson R, Tharp J, and Canning D. Measurement of the bit error rate of an adaptive optics, free-space laser communications systems, part 1: Tip-tilt configuration, Diagnostics, and closed-loop results. Optical Engineering, 2005; 44(9): 096002.

[4] Booth MJ. Adaptive optics in microscopy. Philosophical Transactions Royal Society A, 2007; 365(1098): 2829-2843.

[5] Herrmann J. Least-squares wave front errors of minimum norm. Journal of the Optical Society of America, 1980; 70(1): 28-35.

[6] Freischlad KR, Koliopoulos CL. Modal estimation of a wave front from difference measurements using the discrete Fourier transform. Journal of the Optical Society of America A, 1986; 3(11): 1852–1861.

[7] Poyneer LA, Troy M, Macintosh B, Gavel DT. Experimental validation of Fourier-transform wave-front reconstruction at the Palomar Observatory. Optics Letters 2003; 28(10): 798-800.

[8] Zefreh ZE, Didehvar F, Rajaei A. Accelerated iterative algorithms in reconstruction of computerized tomography images. International Journal of Engineering & Technology Sciences (IJETS), 2014; 2(2): 146-158.

[9] Poyneer LA, Gavel DT, Brase J M. Fast wave-front reconstruction in large adaptive optics systems with use of the Fourier transform. Journal of the Optical Society of America A, 2002; 19(10): 2100–2111.

[10] Roddier F, Roddier C. Wavefront reconstruction using iterative Fourier transforms. Applied Optics, 1991; 30(11): 1325-1327.

[11] Dai G-M. Wavefront Reconstruction from Slope Data Within Pupils of Arbitrary Shapes Using Iterative Fourier Transform. The Open Optics Journal, 2007; 1(1): 1-3.

[12] Tyson RK. Principle of adaptive optics. CRC press 2003.

[13] Roggemann MC, Koivunen AC. Wave-front sensing and deformable-mirror control in strong scintillation. Journal of the Optical Society of America A, 2000; 17(5): 911-919.

[14] Lane RG, Glindemann A, Dainty C. Simulation of a Kolmogorov phase screen. Waves in Random Media, 1992; 2(3): 209-224.

[15] Andrews LC, Phillips RL, Hopen CY. Laser Beam Scintillation with Applications. SPIE Press 2001.